Effect of Discrete Roughness Elements on Flow over Low-Pressure Turbines

Watchapon Rojanaratanangkule

Department of Mechanical Engineering
Chiang Mai University
Chiang Mai 50200, Thailand
watchapon.roj@eng.cmu.ac.th

Richard D. Sandberg

Department of Mechanical Engineering
University of Melbourne
Victoria 3010, Australia
richard.sandberg@unimelb.edu.au

ABSTRACT

In this paper, the influence of an array of discrete roughness elements on the evolution of three-dimensional instabilities of a boundary layer subject to a strong adverse pressure gradient is investigated by means of direct numerical simulation (DNS). The flow configuration is a linear T106 blade cascade with and without roughness elements installed, operating at an isentropic exit Reynolds number of $60,000$ and an exit Mach number of 0.4. The height of the roughness elements considered yields the local roughness Reynolds number of 415, at which steady laminar streamwise vortices form. These steady streaks reduce the size of the suction-side flow separation by accelerating the breakdown process. The streaky vortical structures distort the separated shear layer, resulting in short-span Kelvin–Helmholtz vortices. Further downstream, the streamwise vortices lift the low-momentum fluid from the near-wall region, leading to a strong instability of the streaks and rapid breakdown to turbulence.

INTRODUCTION

Decreasing aerofoil drag is of great importance since it can provide a significant reduction in aircraft fuel burn. In a modern aircraft engine, the low-pressure turbine (LPT) blades generally operate at low Reynolds numbers, ranging from $50,000$ to $500,000$. This results in the flow on most of the suction side being laminar, except in the region close to the trailing edge where flow separation can occur due to an adverse pressure gradient and the separated shear layer typically undergoes rapid transition to turbulence. Reducing the size of the resulting separation bubble is desirable to obtain an increase in the efficiency of the LPT, which can result in a decrease in fuel consumption.

For a typical adverse-pressure-gradient (APG) boundary layer, transition to turbulence occurs via an inflectional inviscid instability. The mechanisms of this instability can be explained as follows. When the flow is decelerating, the velocity profile becomes inflectional. The boundary layer then separates from the surface. This separated shear layer rolls up into two-dimensional coherent vortices, often referred to as 'Kelvin–Helmholtz' (KH) rollers. After the KH rollers break down to turbulence, the separated shear layer reattaches to the surface (for a recent review of various routes to transition of boundary layers in turbine flows, see Coull & Hodson, 2011).

When a single or distributed roughness is placed in a zero-pressure-gradient (ZPG) boundary layer, counter-rotating streamwise vortices appear behind it. This results in an upstream shift of the transition front of an undisturbed boundary layer. The roughness wake vortices can be either steady or unsteady depending on the local roughness Reynolds number $Re_k = u_k k/\nu$, where u_k is the velocity at the roughness height k, and ν is the kinematic viscosity. The critical Reynolds number is in the range between 600 and 900, depending on roughness shape (Klebanoff *et al.*, 1992).

Since roughness elements can accelerate the transition process, they can be employed to APG flow to promote earlier reattachment, which results in a decrease in the size of a separation bubble. Recent numerical works reveal that roughness elements can shorten the bubble if they are placed upstream of the transition point (Rao *et al.*, 2014; Karaca & Gungor, 2016). However, since those simulations investigated the influence of the roughness elements on a flat plate with an adverse pressure gradient, some effects that may appear only in a real blade configuration (e.g. surface curvature or circulation changes) were not included. The aim of this work is to investigate the effect of spanwise periodic arrays of roughness elements on a low pressure turbine blade. The focus is on how the streaky vortical structures alter the inviscid instability of LPT flow.

NUMERICAL APPROACH

The compressible Navier–Stokes equations for conservative variables are solved in curvilinear coordinates via an in-house code, HiPSTAR. The flow solver employs a 4th-order optimised compact central finite-difference scheme (Kim & Sandberg, 2012) to discretise all the spatial derivatives in the axial (x) and pitchwise (y) directions, while a Fourier method is used in the spanwise (z) direction. Temporal advancement is obtained by an ultra-low-storage five-step 4th-order Runge–Kutta scheme (Kennedy *et al.*, 2000). To enhance the stability of the code, a skew-symmetric splitting scheme of the convective terms and a pentadiagonal compact filter (Kim, 2010), applied after every full time-step with a cut-off wavenumber of 0.88, are used. The code has been validated with various benchmark cases and recently been applied to perform DNS of a linear LPT cascade (Sandberg *et al.*, 2015; Michelassi *et al.*, 2015). To represent discrete roughness elements, a second-order boundary data immersion method (BDIM) of Schlanderer *et al.* (2017) is employed.

The reference velocity and length for the LPT DNS are respectively the blade exit velocity u_{2is} and the blade chord length C. Hence, the dimensionless parameters (i.e. Reynolds number Re and Mach number M) are defined based on the blade exit conditions. The Prantdl number and the ratio of the specific heat are set to be constant at $Pr = 0.72$ and $\gamma = 1.4$. The molecular viscosity μ is computed using Sutherland's law with the Sutherland constant of 0.3686. The system of equations is closed by solving the nondimensional equation of state to obtain the pressure.

RESULTS

In this section, the effect of roughness elements on a boundary layer is explored. A simulation of flat-plate flow with roughness elements is first conducted to validate the implementation of the BDIM. Then, results of flow over a LPT blade with and without roughness elements are presented.

Roughness Elements embedded on a Flat Plate

Before exploring the effect of the roughness elements on the real blade geometry, the capability of the numerical technique used to represent a three-dimensional roughness element is first investigated by computing flow over a flat plate with an array of roughness

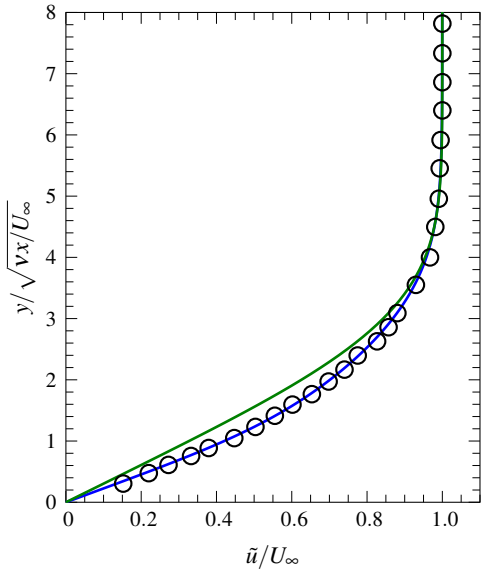

Figure 1. Mean velocity profile at $x = 0.4$ and $z = 0.015$: ○ Bakchinov *et al.* (1995); —— Present; —— Blasius profile.

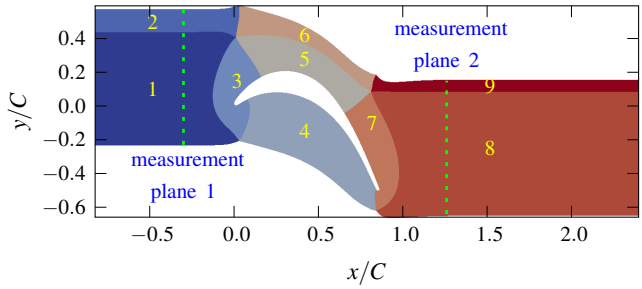

Figure 2. Computational domain of the T106 blade and the multiblock setup used. An O-type grid is employed in blocks 3, 4, 5, and 7 while an H-type grid is used in the remaining blocks.

elements. This precursor simulation is conducted at Mach number of $M = 0.25$, here based on free-stream velocity U_∞. The computational domain has the size $0.22 \le x \le 0.77$, $0 \le y \le 0.025$ and $0 \le z \le 0.03$, with a grid resolution of 782×150 points in the x- and y-directions and 96 Fourier modes in the z-direction. The Blasius solution for the velocity, temperature and density fields are applied at the inlet. The displacement thickness at the inflow boundary is $\delta^* = 1.3652 \times 10^{-3}$, yielding $Re_{\delta^*} = 491.48$. An isothermal no-slip wall is applied at the bottom boundary, while characteristic boundary conditions (CBC) are used at the top boundary. The zonal CBC (Sandberg & Sandham, 2006) is applied to a buffer region extending from $x = 0.62$ to the outflow boundary using 80 points. The spanwise direction is assumed to be periodic. Three rectangular roughness elements, whose dimensions are $0.01 \times 0.0018 \times 0.002$, with spanwise spacing of 0.01, are placed on the flat plate at $x = 0.285$. The roughness element height yields the local roughness Reynolds number of $Re_k = 410.83$. Note that all the parameters in this flat-plate simulation are chosen to match an experiment of Bakchinov *et al.* (1995). The time-averaged streamwise velocity profile is displayed in figure 1, showing that the numerical results are in good agreement with the experimental data (Bakchinov *et al.*, 1995). The Blasius velocity profile is also plotted to illustrate the effect of the roughness elements.

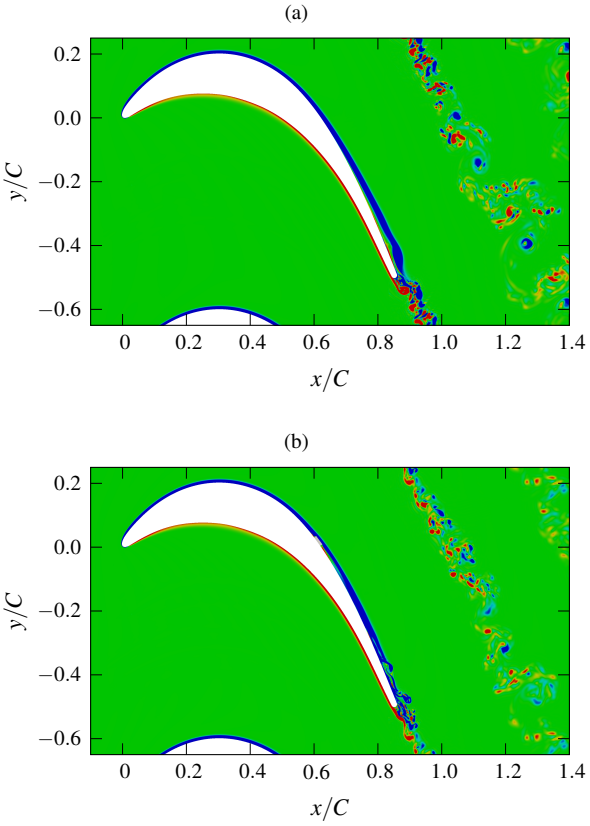

Figure 3. Instantaneous contours of ω_z in the midspan plane ($z/C = 0.1$) for (a) $Re_k = 0$, (b) $Re_k = 415$. Vorticity varies from $-50 < \omega_z < 50$. Blue and red patches respectively show negative and positive vorticity.

DNS of LPT Blade with Roughness Elements

In this work, the T106 blade operating at an isentropic exit Reynolds number of about 60,000 and an exit Mach number of 0.4 is considered. Figure 2 displays the computational domain of the T106 blade and the multiblock setup used. The spanwise extent is 20% of the blade chord length. The stagger angle is 30.7°, thus the blade axial chord length is $C_{ax} = C\cos(30.7°)$. At the inlet boundary, a sponge layer is applied to force the flow solution to a target state, while the zonal characteristic boundary conditions are employed at the outlet. Periodic boundary conditions are used in the pitchwise and spanwise directions. The blade surface is treated as a no-slip isothermal wall. Three roughness elements are placed on the suction side at $x/C_{ax} = 0.7$ with the width of 0.02 and the distance between the elements of $\lambda_z = 0.067$. Two cases with different roughness heights, corresponding to the local roughness Reynolds number of 0 (i.e. no roughness elements) and 415 are considered.

The simulations are conducted with an in-plane grid count of about 2.6×10^5. The number of Fourier mode in the spanwise direction for these two cases is different. For the LPT blade without the roughness elements (i.e. $Re_k = 0$), 32 Fourier modes are employed, resulting in the total number of grid cells being the same as the previous DNS of Sandberg *et al.* (2015). To adequately resolve the streamwise vortices induced by the roughness elements, 96 Fourier modes are applied. Thus the total grid count is 50.4×10^6 points. It should be noted that on the suction side the first wall-normal grid point in plus units is located below unity after 60% of the blade chord length. Upstream of that Δy_1^+ is less than 1.4, which is sufficient to capture a laminar boundary layer. The grid resolution in the streamwise and spanwise directions is respectively $\Delta x^+ < 10$ and $\Delta z^+ < 12.64$ in the laminar region, while those in the transitional flow region are $\Delta x^+ < 4$ and $\Delta z^+ < 3.14$. To obtain statistical

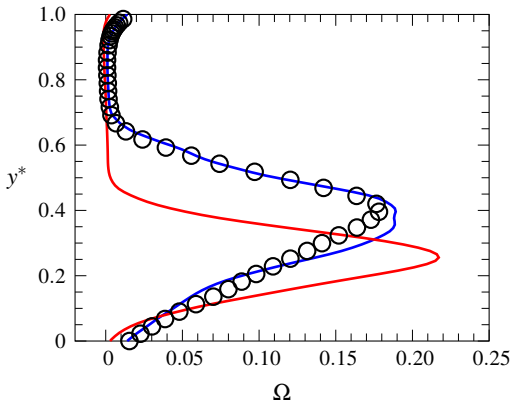

Figure 4. Time-averaged wake loss profiles at $x/C = 1.26$: ○ Michelassi *et al.* (2015); —— $Re_k = 0$; —— $Re_k = 415$. The turbulence intensity measured at $x/C = -0.3$ for each case is respectively $Tu = 0.5\%, 0.42\%, 0.09\%$.

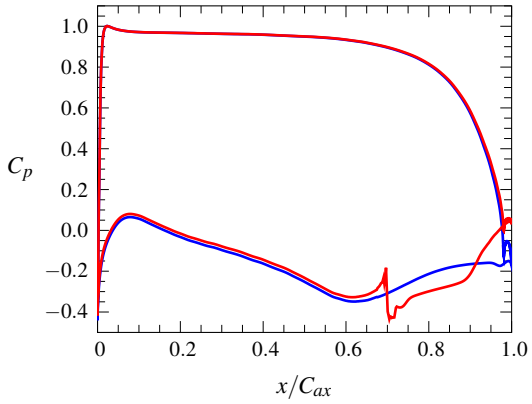

Figure 5. Time-averaged pressure coefficient on the blade surface for (a) —— $Re_k = 0$, (b) —— $Re_k = 415$.

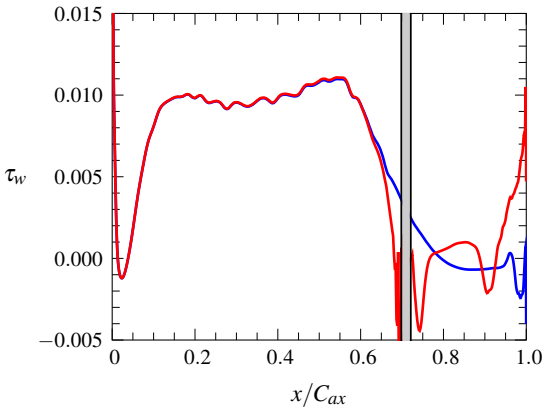

Figure 6. Time-averaged wall shear stress on the blade suction side for (a) —— $Re_k = 0$, (b) —— $Re_k = 415$. The grey area indicates the location of the roughness elements.

data, the simulations are time averaged for the last five flow-through times.

Figure 3 shows contours of the instantaneous spanwise vorticity ω_z in the midspan plane. Without the roughness elements (figure 3a), a large vortical structure (i.e. Kelvin–Helmholtz roller) forms in the aft section of the suction side. This coherent structure results from the flow separation due to an adverse pressure gradient and leads to a rapid breakdown to turbulence. Once the roughness elements are installed, the KH rollers seem to form farther upstream, leading to earlier breakdown, as illustrated in figure 3(b). The turbulent wake shed behind the blade for this case seems to be less organised compared to the case of $Re_k = 0$. The time-averaged wake loss profile at $x/C = 1.26$ along the nondimensional pitchwise direction y^* is displayed in figure 4. The wake loss is defined as $\Omega = \left(p^A_{t,1} - p_{t,2}(y^*)\right) / \left(p^A_{t,1} - p^A_2\right)$, where $p^A_{t,1}$ is the mass-flow-averaged stagnation pressure at $x/C = 0.3$, $p_{t,2}$ is the stagnation pressure at $x/C = 1.26$ and p^A_2 is the mass-flow-averaged pressure at $x/C = 1.26$. The wake loss profile from the DNS of Michelassi *et al.* (2015) is also plotted to verify the correctness of the case $Re_k = 0$. The distribution of Ω is found to agree well with the previous DNS (Michelassi *et al.*, 2015) although some minor discrepancies near the peak can be observed due to a difference in the inlet turbulence intensity Tu. However, the roughness case is conducted with the same inlet conditions as the present smooth wall DNS. When the roughness elements are employed ($Re_k = 415$), an increase in the peak magnitude is obtained, while the width of the wake loss profile decreases. This results in a decrease in the total, or integral, mixed-out loss ($\int \Omega \, \mathrm{d}y^*$) from 0.066 ($Re_k = 0$) to 0.046 ($Re_k = 415$).

The location where the boundary layer separates and reattaches can be seen from the plot of the blade pressure coefficient $C_p = \left(p_w - p^A_2\right) / \left(p^A_{t,1} - p^A_2\right)$ (figure 5) and wall shear stress $\tau_w = \mu \partial u_t / \partial y_n$ (figure 6), where p_w is the pressure along the blade surface, u_t is the velocity tangential to the blade surface and y_n is the wall-normal direction. For both cases, C_p on the pressure side is approximately the same and the flow does not separate on this side. In contrast, the flow on the suction side decelerates after $x/C_{ax} \approx 0.6$, leading to flow separation and reattachment. The location of a laminar separation bubble can be marked by either the plateau near the trailing edge of the C_p plot or a negative value of τ_w. For the case of $Re_k = 0$, the flow begins to separate at $x/C_{ax} \approx 0.79$ and reattaches at $x/C_{ax} \approx 0.95$, yielding a bubble length of about 0.16. When the roughness elements are installed, a small region of reverse flow appears immediately behind them. The boundary layer separates again at $x/C_{ax} \approx 0.89$ and quickly reattaches at $x/_{ax} \approx 0.93$, yielding a dramatic increase in C_p and τ_w. This suggests that the boundary layer becomes turbulent after that location.

To help explain the effect of the roughness elements on the flow, instantaneous flow structures are visualised by means of the second invariant of the velocity gradient tensor $Q = -0.5 u_{i,j} u_{j,i}$ (for details see Jeong & Hussain, 1995) in figure 7. Without the roughness elements ($Re_k = 0$), the separated shear layer rolls up into spanwise coherent KH rollers and breaks down into small-scale structures very close to the trailing edge (figure 7a). For the case of $Re_k = 415$, the roughness elements generate longitudinal streamwise vortices that seem to be steady, which can be seen from contours of ω_x on a plane parallel to the blade suction surface (figure 7b). These streamwise vortices distort the separated shear layer, resulting in three-dimensional coherent vortices. The short-span KH-like vortices rapidly break down to smaller flow structures. Note that this route to transition is similar to the breakdown due to the 'Klebanoff modes' which occurs when a laminar boundary layer is subject to free-stream turbulence (Coull & Hodson, 2011).

The topology of the streaky vortical structures is displayed in figure 8(a). The isosurfaces of the instantaneous ω_x show that horseshoe vortices appear in front of the roughness elements, while two counter-rotating vortex pairs are encountered downstream. The inner vortex pair decays after some streamwise distance, while the outer one convects further downstream and breaks down to a turbu-

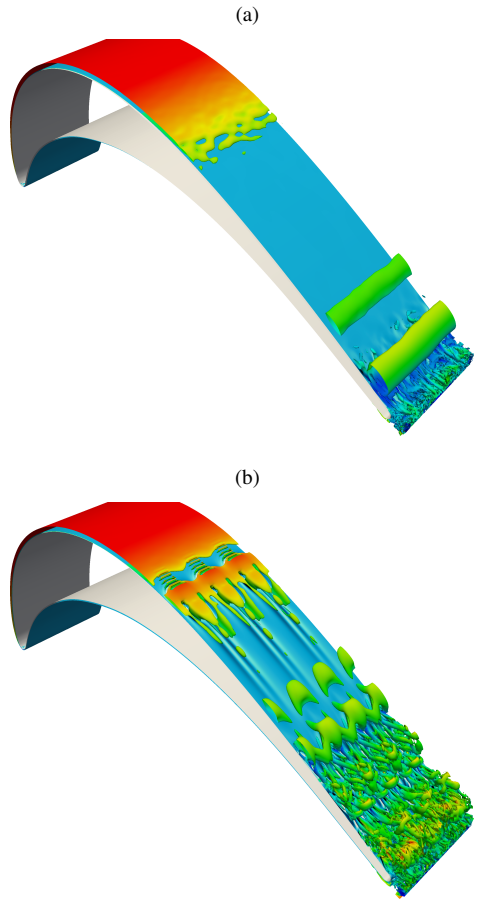

Figure 7. Instantaneous coherent structures, visuallised by isosurfaces of Q, of flow over the LPT blade at (a) $Re_k = 0$ and (b) $Re_k = 415$. The contour of ω_x near the suction surface illustrates the presence of the longitudinal streamwise vortices induced by the roughness elements.

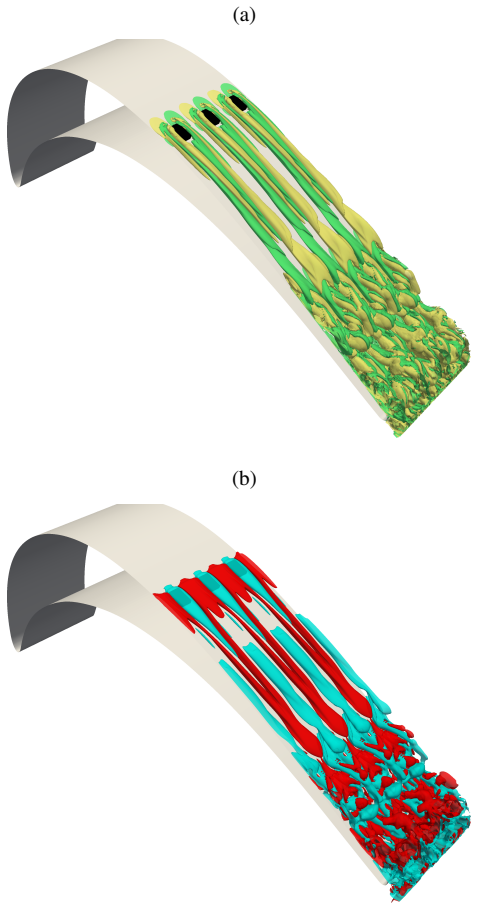

Figure 8. The formation of (a) instantaneous streamwise vortices (yellow and green patches respectively show positive and negative vorticity) and (b) low- (blue) and high-speed (red) streaks at $Re_k = 415$.

lent boundary layer. The evolution of the streamwise streaks is relevant to the longitudinal vortices. Immediately upstream and downstream of each roughness element, two regions of separated flow are induced, while the high-speed streak forms between the roughness elements (figure 8b). The contour plot of the instantaneous streamwise fluctuating velocity u' at various streamwise locations is also given in figure 9 to clarify the formation of the streaks. The legs of the high-speed streak merge with each other when they evolve downstream, leading to a shift of their position to be located in correspondence to the roughness elements, as displayed in figures 9(a)–9(d). In the meantime, the low-speed streak disappears and regenerates in the free space between the roughness elements. Further downstream, the low-momentum fluid is lifted up away from the wall by the longitudinal vortices (figure 9e), resulting in strong algebraic growth of boundary layer streaks and breakdown to turbulence.

The wall-normal distribution of the Favre-averaged tangential velocity $\tilde{u}_t$ is given in figure 10(a). The profile of $\tilde{u}_t$ reveals a strong reverse flow behind the roughness elements. The inflection point seems to shift towards the wall, indicating that the boundary layer becomes attached. This confirms that the roughness elements can reduce the size of the separation bubble. Figure 10(b) shows profiles of turbulence kinetic energy (TKE). The wall-normal location of the maximum TKE is shown by a white circle in the figure. It can be seen that the magnitude of the TKE increases with streamwise distance up to $x/C_{ax} = 0.7988$. After that location, the TKE decreases, presumably because the merging of the high-speed streak is completed. The TKE then increases again at $x/C_{ax} = 0.8856$.

The spanwise variation of the fluctuating tangential velocity $\tilde{u}_t' = \tilde{u}_t - \langle \tilde{u}_t \rangle_z$ taken at the peak location of the TKE, and its spectrum are shown in figure 11. For the streamwise streaks induced by an array of roughness elements, the most dominating spanwise wavelength is expected to be equal to the distance between each roughness element. Downstream of the roughness elements, although the wavelength of 0.067 has the highest energy, its higher harmonics also contain a significant amount of energy. This results in the sinusoidal modulation of $\tilde{u}_t'$ as displayed in figure 11(a). While the low-speed streak decays, the energy of $\lambda_z = 0.067$ is much lower (about 4 orders of magnitude) than its third harmonic (figure 11b). The wavelength of $\lambda_z = 0.067$ has the highest energy again during the merging of the high-speed streak (figures 11c–11d) and the lift-up process (figure 11e). The spectra plots indicate that an array of roughness elements is efficient at generating spanwise disturbances at specific wavelengths. In the present work, the four dominant wavelengths are 0.067, 0.033, 0.022 and 0.0167, corresponding to $\lambda_{z,0}$, $\lambda_{z,0}/2$, $\lambda_{z,0}/3$ and $\lambda_{z,0}/4$, respectively.

SUMMARY

The effect of longitudinal streamwise streaks induced by discrete roughness elements on flow over a low pressure turbine blade is investigated using DNS. The focus is on the interaction between the streaky vortices with an inviscid Kelvin–Helmholtz instability. The prominent effect of the roughness elements is an upstream shift

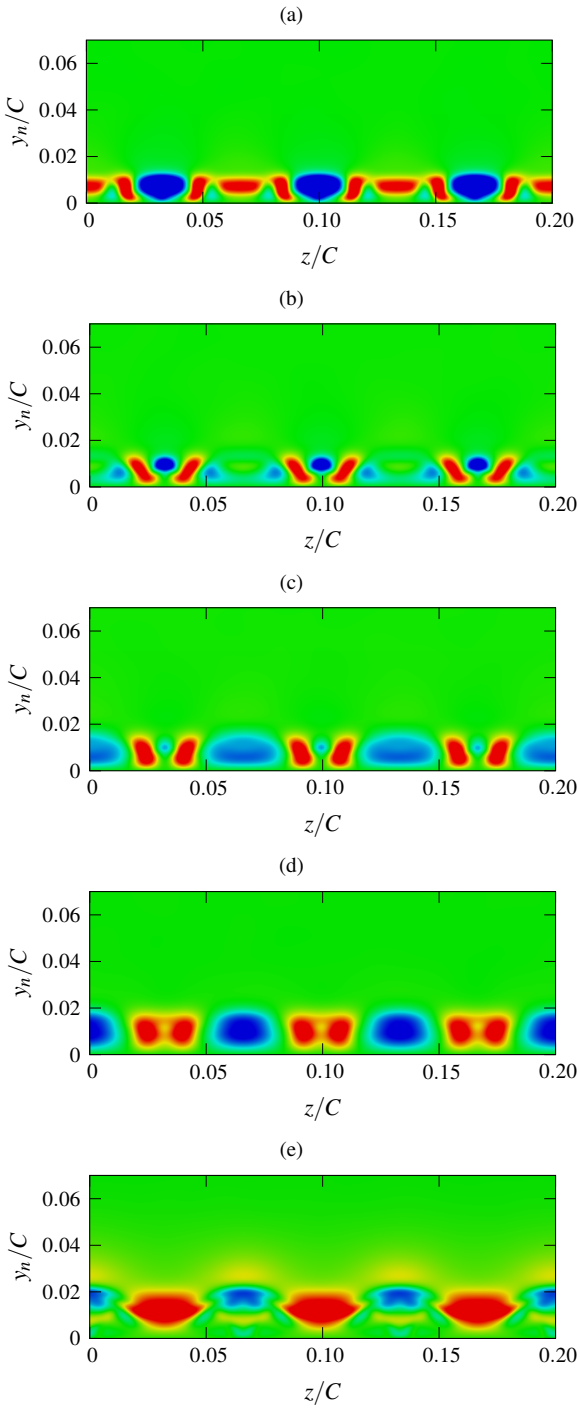

Figure 9. Instantaneous contours of u' for $Re_k = 415$ at (a) $x/C_{ax} = 0.7426$, (b) $x/C_{ax} = 0.7705$, (c) $x/C_{ax} = 0.7988$, (d) $x/C_{ax} = 0.8434$ and (e) $x/C_{ax} = 0.8856$. Fluctuating velocity varies from $-0.15 < u' < 0.15$. Blue and red patches respectively show negative and positive velocity.

of the breakdown to turbulence, which leads to a reduction in the size of a separation bubble and a decrease in the total mixed-out loss. The low- and high-speed streaks distort the KH rollers into a sinusoidal modulation with the most dominant wavelength equal to the spanwise distance of each roughness element. The low-speed streak is lifted up away from the wall by the streamwise vortices, resulting in the rapid breakdown to turbulence. Future work will investigate how the instability mechanisms of LPT flows are altered by the combined effect of an incoming wake and spanwise arrays of roughness elements.

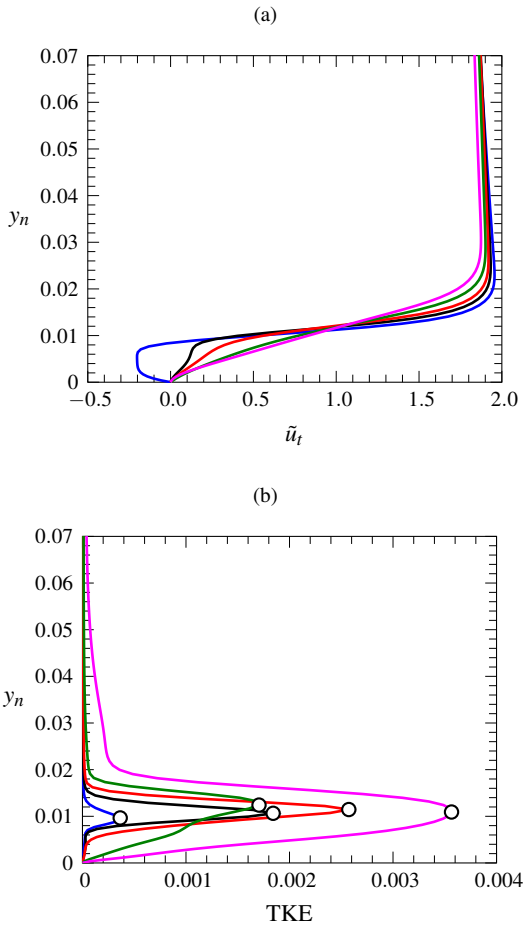

Figure 10. Profiles of (a) time-averaged tangential velocity and (b) turbulence kinetic energy along wall-normal distance: $x/C_{ax} = 0.7426$, $x/C_{ax} = 0.7705$, $x/C_{ax} = 0.7988$, $x/C_{ax} = 0.8434$, $x/C_{ax} = 0.8856$. The circles mark the peak wall-normal position of turbulence kinetic energy.

ACKNOWLEDGMENTS

This work is supported by the Thailand Research Fund (TRF) and the Endeavour Research Fellowships. The computational resources from the Pawsey Supercomputing Centre in Western Australia and the National Computational Infrastructure (NCI) supported by the Australian Government are appreciated.

REFERENCES

Bakchinov, A. A., Grek, G. R., Klingmann, B. G. B. & Kozlov, V. V. 1995 Transition experiments in a boundary layer with embedded streamwise vortices. *Phys. Fluids* **7** (4), 820–832.

Coull, J. D. & Hodson, H. P. 2011 Unsteady boundary-layer transition in low-pressure turbines. *J. Fluid Mech.* **681**, 370410.

Jeong, J. & Hussain, F. 1995 On the identification of a vortex. *J. Fluid Mech.* **285**, 69–94.

Karaca, S. & Gungor, A. G. 2016 DNS of unsteady effects on the control of laminar separated boundary layers. *Eur. J. Mech. B-Fluids* **56**, 71–81.

Kennedy, C. A., Carpenter, M. H. & Lewis, R. M. 2000 Low-storage, explicit Runge–Kutta schemes for the compressible Navier–Stokes equations. *Appl. Numer. Math.* **35** (3), 177–219.

Kim, J. W. 2010 High-order compact filters with variable cut-off wavenumber and stable boundary treatment. *Comput. Fluids* **39** (7), 11681182.

Kim, J. W. & Sandberg, R. D. 2012 Efficient parallel computing

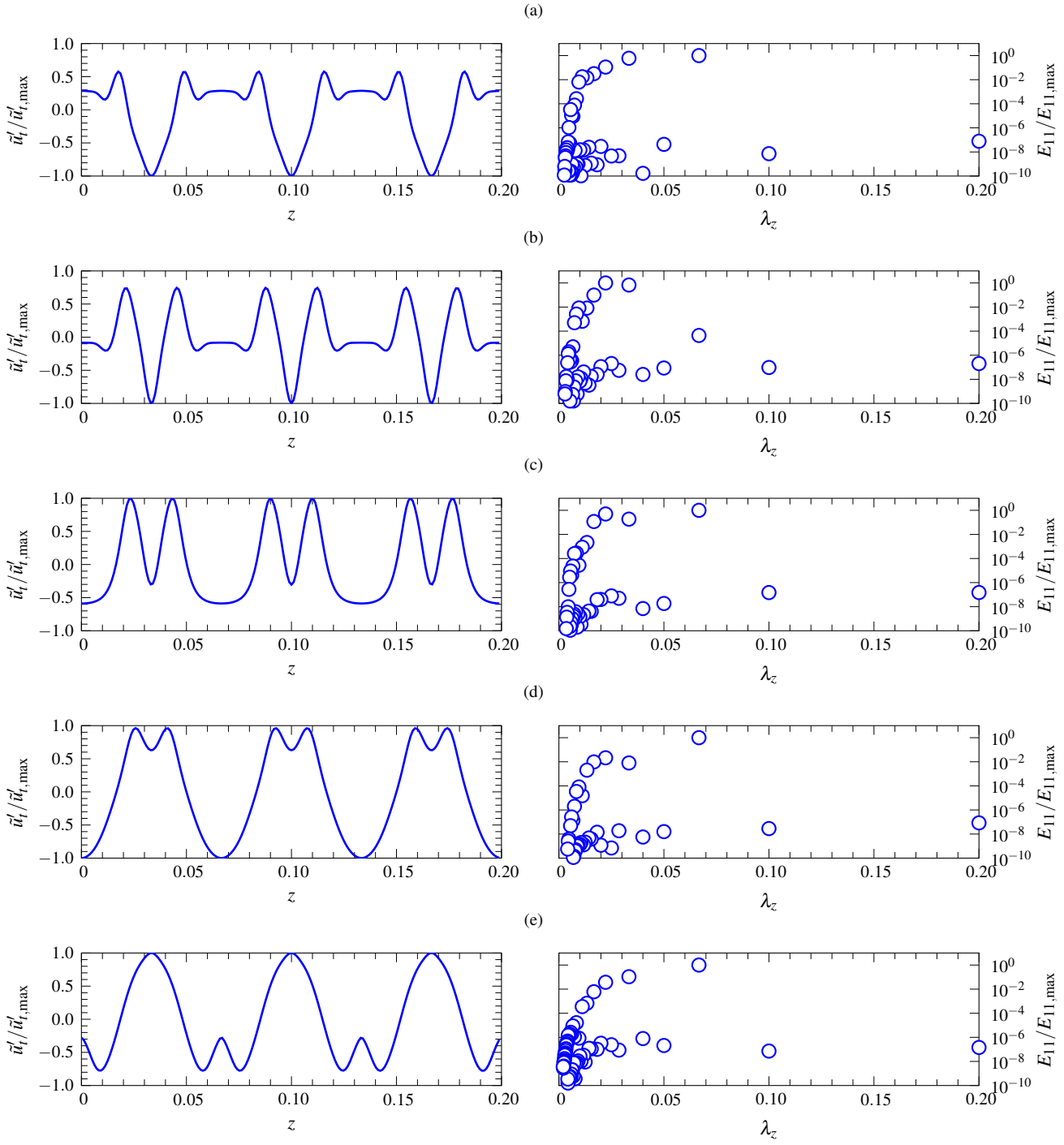

Figure 11. Spanwise distribution of (left) $\tilde{u}_t'$ taken at the TKE peak and normalised to ± 1 and (right) its spectra at (a) $x/C_{ax} = 0.7426$, (b) $x/C_{ax} = 0.7705$, (c) $x/C_{ax} = 0.7988$, (d) $x/C_{ax} = 0.8434$ and (e) $x/C_{ax} = 0.8856$.

with a compact finite difference scheme. *Comput. Fluids* **58**, 70–87.

Klebanoff, P. S., Cleveland, W. G. & Tidstrom, K. D. 1992 On the evolution of a turbulent boundary layer induced by a three-dimensional roughness element. *J. Fluid Mech.* **237**, 101–187.

Michelassi, V., Chen, L., Pichler, R. & Sandberg, R. D. 2015 Compressible direct numerical simulation of low-pressure turbines. Part II: Effect of inflow disturbances. *J. Turbomach.* **137** (7), 071005.

Rao, V. N., Jefferson-Loveday, R., Tucker, P. G. & Lardeau, S. 2014 Large eddy simulations in turbines: Influence of roughness and free-stream turbulence. *Flow Turbul. Combust.* **92** (1), 543–561.

Sandberg, R. D., Michelassi, V., Pichler, R., Chen, L. & Johnstone, R. 2015 Compressible direct numerical simulation of low-pressure turbines. Part I: Methodology. *J. Turbomach.* **137** (5), 051011.

Sandberg, R. D. & Sandham, N. D. 2006 Nonreflecting zonal characteristic boundary condition for direct numerical simulation of aerodynamic sound. *AIAA J.* **44** (2), 402405.

Schlanderer, S. C., Weymouth, G. D. & Sandberg, R. D. 2017 The boundary data immersion method for compressible flows with application to aeroacoustics. *J. Comput. Phys.* **333**, 440461.